Rare Metal Materials and Engineering
Volume 51, Issue 4, April 2022
Available online at www.rmme.ac.cn

Science Press

Cite this article as: Lang Ruiqing, Han Yongquan, Bai Xueyu, et al. Impacting Mechanism of Variable Polarity Frequency on Weld Pool Stability in Variable Polarity Plasma Arc Keyhole Vertical Welding of Aluminum Alloy[J]. Rare Metal Materials and Engineering, 2022, 51(04): 1172-1182.

ARTICLE

Impacting Mechanism of Variable Polarity Frequency on Weld Pool Stability in Variable Polarity Plasma Arc Keyhole Vertical Welding of Aluminum Alloy

Lang Ruiqing, Han Yongquan, Bai Xueyu, Bao Xulei

Inner Mongolia University of Technology, Hohhot 010051, China

Abstract: To study the impacting mechanism of variable polarity frequency (VPF) on the weld pool stability in variable polarity plasma arc welding (VPPAW), the thermal-mechanical coupling process of the keyhole weld pool was analyzed by a variable-polarity finite element model. The model was developed based on the computational fluid dynamics (CFD), which can realize the periodic variation of thermal and mechanical effects of variable polarity arc on the weld pool. Moreover, in order to more accurately express the heat and force distribution on the keyhole boundary along the keyhole depth, the secondary compression effect of the keyhole on heat flux and arc pressure was taken into account. The thermal-mechanical "oscillations intensity" on the keyhole boundary and the force balance of the molten bridge were compared at different VPFs. The results show that the "oscillation intensity" of the arc pressure, heat flux and the flow velocity on the keyhole boundary decreases with increasing the VPFs during the keyhole formation. In addition, the variation of the temperature field in the weld pool caused by different thermal-mechanical oscillations results in the change of surface tension and the force balance condition of the molten bridge is changed, which affects the keyhole weld pool stability. When the VPFs are more than 33 and less than 83 and the duty radio of current in EP phase is 1/5, the thermal-mechanical "oscillations intensity" on the keyhole boundary is weak, and the molten bridge can stay force balance in the critical state of being penetrated, so the weld pool can maintain stable. When the VPFs are less than 33, the "oscillations intensity" is strong and the force balance of the molten bridge is broken, and the weld tends to be cut. If the VPFs are more than 83, the weld pool is unstable due to the broken force balance of the molten bridge although the "oscillations intensity" is weak. Finally, the accuracy of the developed model was verified by the comparison of the fusion zone, the keyhole penetration time and keyhole dimensions on the backside of the weld.

Key words: VPPAW; VPF; keyhole compression effect; thermal-mechanical oscillation; weld pool stability

VPPAW has great application potential in aluminum alloys welding, which can be used to realize the double-sided formation through single-sided welding, and the oxide film on the surface of aluminum alloy can be cleaned by cathode atomization[1]. VPPA vertical welding is regarded as a primary welding technique for many important structural components in space and aeronautics[2,3]. Yao et al[4] proposed that the welding process of FSW, VPPA and VPTIG can be applied comprehensively to realize the weld with low stress, nearly no distortion and military defects of the key structure of propellant tank. However, the stability of the keyhole weld pool is poor, resulting in a much narrower parameter window compared to conventional methods.

With the typical asymmetric square waveform of the welding current, the outstanding feature of VPPAW is that the negative and positive polarity current, time and plasma gas flow can be adjusted independently. Due to the complexity of its physical process, the research on VPPA keyhole vertical welding of aluminum alloy mainly adopts experimental method, and the theoretical analysis is less. Han et al[5] studied the characteristics of arc stability and energy transfer in VPPAW. Scholars[6-8] reported the influence of welding current and plasma gas flow rate on weld formation. In these experimental studies, the VPFs between 40 and 48 were recommended, but the impacting mechanism of VPF on weld pool stability has rarely been reported.

Received date: April 02, 2021
Foundation item: National Natural Science Foundation of China (51665044)

Corresponding author: Han Yongquan, Ph.D., Professor, School of Materials Science and Engineering, Inner Mongolia University of Technology, Hohhot 010051, P. R. China, Tel: 0086-471-6575752, E-mail: hyq@imut.edu.cn

In VPPA welding process, the arc during EN phase acts on the center of the weld pool to achieve deep and narrow penetration. The heating area of the arc in EP phase is larger than that of EN phase[9]. VPPA switches the positive and negative polarity at high speed under high constraint state, which will cause the thermal-mechanical oscillation on the keyhole boundary. The variable polarity time has a great influence on the central arc pressure and the excessive central pressure will destroy the weld pool stability[10]. Pei et al[11] confirmed that the temperature distribution at the time of penetration is the decisive factor affecting the stable forming of arc striking. However, the weld pool involves complex thermal-mechanical coupling process. Obviously, it is not comprehensive to analyze the weld pool stability from the point of central arc pressure or temperature distribution of the weld pool alone.

The oscillation of heat flux and flow velocity at the keyhole boundary is difficult to detect with the current detection methods. In recent years, numerical simulation can be used to understand the mechanism and physical interaction of various welding processes[12]. In plasma arc welding (PAW) of stainless steel, the shear force is the dominant driving force for the weld pool flow, and the keyhole dimension has a clear effect on metal flow[13,14], which contributes to targeted stability control. However, due to differences in material properties and arc output, the keyhole weld pool dimensions and flow pattern of the VPPA welding of aluminum alloys are different from those of the PAW of stainless steel[10,15]. Yang et al[16-18] analyzed the material flow behavior in the weld pool during the keyhole evolution of aluminum alloy with 6 mm in thickness. Nevertheless, the variation in heat and force output of the arc in EN and EP phase was ignored in modeling. The keyhole has secondary compression effect on heat flux and arc pressure in PAW process[14,19]. However, the above studies did not consider the keyhole secondary compression effect.

In this work, a variable-polarity model was established, which realizes the heat and force variation of the VPPA and the secondary compression effect of keyhole on heat flux and arc pressure. The impacting mechanism of VPF on the weld pool stability was revealed from the perspective of thermal-mechanical oscillation at the keyhole boundary and the force balance of molten bridge.

1 Experiment

The VPPA vertical welding system is schematically shown in Fig. 1, which consists of a welding power source (VPPA-3), plasma arc welding torch (PAW-300), water-cooling facility, automatic wire feeder and high-speed camera (Red Lake Y4) etc. The workpiece employed was a 2A14 aluminum alloy (AA2A14) with a dimension of 120 mm×60 mm×12 mm (length×width×thickness). The welding parameters are summarized in Table 1[5]. The chemical composition of the base metal and wire[20,21] is shown in Table 2.

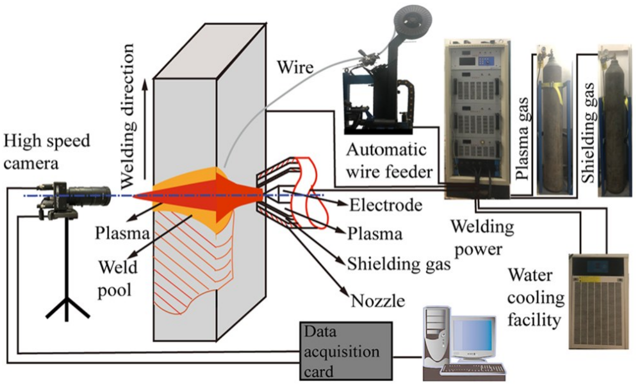

Fig.1 Schematic diagram of experimental setup

Table 1 VPPAW process parameters[5]

Parameter	Value	Remark
I_0/A	180	Preheating current
t_0/s	2	Preheating time
I_{EN}/I_{EP}	240/280	Current in EN and EP phase
$t_{EN}/(t_{EN}+t_{EP})$	5/1	Duty radio of current in EN phase
t_{EN}/t_{EP}	30/6	Case a
	25/5	Case b
	20/4	Case c
	10/2	Case d
	5/1	Case e
Q/L·min^{-1}	3	Plasma gas flow rate
Q_s/L·min^{-1}	15	Flow rate of shielding gas
v/mm·min^{-1}	120	Welding speed
v_w/mm·min^{-1}	2.8	Wire feeding speed
U_{EN}/U_{EP}	26/30	Arc voltage in EN phase and EP phase
d/mm	4.0	Nozzle diameter
ι/mm	6	Distance from torch to workpiece

Table 2 Chemical composition of AA2A14 and ER4043 (wt%)[20,21]

Material	Cu	Mg	Mn	Fe	Si	Ti	Zn	Al
AA2A14	3.9~4.8	0.4~0.8	0.4~1.0	≤0.7	0.6~1.2	≤0.15	≤0.3	Bal.
ER4043	≤0.3	≤0.05	≤0.05	≤0.8	4.5~6.0	≤0.2	≤0.1	Bal.

2 Modeling and Simulation Consideration

2.1 Model description

The related physical parameters are shown in Table 3. The mathematical model was developed by introducing the following assumptions.

(1) Molten metal is considered as a laminar incompressible Newtonian fluid affected by the plasma arc pressure, surface tension, electromagnetic force and gravity[22].

(2) A Boussinesq approximation was used to treat the buoyancy term[23].

Table 3 Nomenclature

Symbol	Physical interpretation
T_s/K	Solid temperature
T_l/K	Liquid temperature
T_b/K	Boiling temperature
T_0/K	Reference temperature
μ_0	Magnetic permeability
I/A	Welding current
σ_j/m	Current distribution parameter
h_{hk}/m	Keyhole depth
C_j	Adjustment factor of the arc pressure
r/m	Radius
r_p/m	Plasma arc radius on the workpiece
r_0/N·m^{-2}·K^{-1}	Temperature coefficient
h_c/W·m^{-2}·K^{-1}	Convective heat transfer coefficient
σ/W·m^{-2}·K^{-1}	Stefan-Boltzmann constant
ε	Radiation emissivity
L_m/J·kg^{-1}	Latent heat of fusion
C_pJ·kg^{-1}·K^{-1}	Specific heat
x, y, z/m	Coordinate of x, y and z axes
L/m	Workpiece thickness
κ/W·m^{-1}·k^{-1}	Thermal conductivity
m_1, m_2, f_1, f_2	Energy distribution coefficient

(3) The thermal conductivity, specific heat, surface tension and viscosity are related to temperature, whereas the other thermo-physical parameters are constant[24].

The continuous equation[25] can be expressed through Eq.(1):

$$\partial\rho/\partial t + \nabla \cdot \rho\vec{v} = 0 \tag{1}$$

where ρ is the mixture density, t is the time, $\vec{v}$ is the velocity vector.

The momentum conservation equation[26] in the x, y, z directions can be written as follows:

$$\rho\left[\frac{\partial u}{\partial t} + u\frac{\partial u}{\partial x} + v\frac{\partial u}{\partial y} + w\frac{\partial u}{\partial w}\right] = -\frac{\partial p}{\partial x} + \mu\left(\frac{\partial^2 u}{\partial x^2} + \frac{\partial^2 u}{\partial y^2} + \frac{\partial^2 u}{\partial z^2}\right) + S_x \tag{2}$$

$$\rho\left[\frac{\partial v}{\partial t} + u\frac{\partial v}{\partial x} + v\frac{\partial v}{\partial y} + w\frac{\partial v}{\partial w}\right] = -\frac{\partial p}{\partial y} + \mu\left(\frac{\partial^2 v}{\partial x^2} + \frac{\partial^2 v}{\partial y^2} + \frac{\partial^2 v}{\partial z^2}\right) + S_y \tag{3}$$

$$\rho\left[\frac{\partial w}{\partial t} + u\frac{\partial w}{\partial x} + v\frac{\partial w}{\partial y} + w\frac{\partial w}{\partial w}\right] = -\frac{\partial p}{\partial z} + \mu\left(\frac{\partial^2 w}{\partial x^2} + \frac{\partial^2 w}{\partial y^2} + \frac{\partial^2 w}{\partial z^2}\right) + S_z \tag{4}$$

where u, v, and w are the velocity in x, y, and z directions, respectively, ρ is the mixture density, and μ is the viscosity.

The momentum source terms S_x, S_y and S_z can be expressed as follows:

$$S_x = A_x + F_x \tag{5}$$

$$S_y = A_y + F_y \tag{6}$$

$$S_z = A_z + F_z + P_a' \tag{7}$$

where A_x, A_y and A_z are the momentum loss in the solid-liquid two-phase region; F_x, F_y, F_z are the electromagnetic force in the x, y and z direction, respectively; P_a' is the arc pressure.

The momentum loss of a solid-liquid zone is treated by an enthalpy-porosity technique[27], and calculated as follows:

$$A_x = -A_{\text{mush}}(1-\beta)^2 u/(\beta^2 + \xi) \tag{8}$$

$$A_y = -A_{\text{mush}}(1-\beta)^2 v/(\beta^2 + \xi) \tag{9}$$

$$A_z = -A_{\text{mush}}(1-\beta)^2 w/(\beta^2 + \xi) \tag{10}$$

where A_{mush} is the mushy zone constant, β is the volume fraction of the liquid phase, and ξ is the non-zero decimal denominator. The relationship between β and temperature T is shown as follows:

$$\beta = \begin{cases} 0, & T \leqslant T_s \\ 1, & T \geqslant T_l \\ (T - T_s)/(T_l - T_s), & T_s < T < T_l \end{cases} \tag{11}$$

The electromagnetic forces are expressed as follows:

$$F_x = -\frac{\mu_0 I^2}{4\pi^2\sigma_j^2 r}\exp\left(-\frac{r^2}{2\sigma_j^2}\right)\left[1-\exp\left(-\frac{r^2}{2\sigma_j^2}\right)\right]\left(1-\frac{z}{L}\right)^2\frac{x}{r} \tag{12}$$

$$F_y = -\frac{\mu_0 I^2}{4\pi^2\sigma_j^2 r}\exp\left(-\frac{r^2}{2\sigma_j^2}\right)\left[1-\exp\left(-\frac{r^2}{2\sigma_j^2}\right)\right]\left(1-\frac{z}{L}\right)^2\frac{y}{r} \tag{13}$$

$$F_z = -\frac{\mu_0 I^2}{4\pi^2\sigma_j^2 r}\exp\left(-\frac{r^2}{2\sigma_j^2}\right)\left[1-\exp\left(-\frac{r^2}{2\sigma_j^2}\right)\right]\left(1-\frac{z}{L}\right) \tag{14}$$

where $r=(x^2+y^2)^{-1/2}$.

The energy conservation[26] can be expressed through Eq.(15):

$$\rho c_p\left[\frac{\partial T}{\partial t} + u\frac{\partial T}{\partial x} + v\frac{\partial T}{\partial y} + w\frac{\partial T}{\partial z}\right] = \frac{\partial}{\partial x}\left(\kappa\frac{\partial T}{\partial x}\right) + \frac{\partial}{\partial y}\left(\kappa\frac{\partial T}{\partial y}\right) + \frac{\partial}{\partial z}\left(\kappa\frac{\partial T}{\partial z}\right) + S_H + S_v \tag{15}$$

where S_H is the energy change caused by the liquid phase transition and $S_H = h_{\text{ref}} + \int_{T_0}^{T} C_p \, dT + \Delta H$ in which $\Delta H = \beta L_m h_{\text{ref}}$ is the reference enthalpy; S_v is the heat source.

2.2 Keyhole tracking

A two-phase (gas and aluminum alloy) flow model was used[28].

$$\partial F/\partial t + (\nabla \cdot \vec{v}) \cdot F = 0 \tag{16}$$

where volume fraction function F=1 corresponds to cell that is full of metal fluid, while F=0 corresponds to cells without metal fluid. Cells with F between 0 and 1 locate in the free surface.

2.3 Boundary conditions

The plasma/liquid interface is free surface, on which the normal pressure balance is expressed as follows[22]:

$$-P + 2\mu \cdot \frac{\partial \vec{v}_n}{\partial \vec{n}} = -P_a' + \gamma \cdot \left(\frac{1}{R_1} + \frac{1}{R_2}\right) \tag{17}$$

where P is the liquid pressure in the normal direction, μ is the dynamic viscosity, P_a' is the improved arc pressure, $\vec{v}_n$ is the velocity vector, R_1 and R_2 are the principal radii of curvature of the free surface, $\vec{n}$ is the normal component, γ is the surface tension which is adopted using the continuum surface force (CSF) model[29] and calculated as follows[18]:

$$\gamma = \begin{cases} 0.825 & T = T_s \\ 0.825 - 0.5 \times 10^{-4} T & T_l < T < T_b \end{cases} \tag{18}$$

where T is the real-time temperature of the weld pool.

In consequence of the variation of surface tension coefficient with temperature gradient, Marangoni shear stress $\tau_{\vec{s}}$ at the free surface can be described as follows:

$$\tau_{\vec{s}} = -\mu \frac{\partial v_s}{\partial \vec{n}} = -\frac{\mathrm{d}(\gamma)}{\mathrm{d}T} \cdot \frac{\partial T}{\partial \vec{s}} \tag{19}$$

where $\vec{s}$ is the tangential component of the free surface.

Fig. 2 shows a schematic diagram of the surface boundary, the conditions are set as indicated in Table 4, where $\partial T/\partial \vec{n}$ is the temperature gradient, $\partial T/\partial \vec{y}$ is the variance ratio of temperature along the y axis; $\partial u/\partial \vec{y}$ and $\partial w/\partial \vec{y}$ are the velocity variation rates along the y and z axes, respectively. The actual heat dissipation is simulated by setting the heat transfer coefficient and thermal emissivity.

2.4 Heat input during VPPAW process

Fig.3 shows that the arc distribution range in the EN phase is more concentrated than in the EP phase, which is caused by the gradual cleaning of the oxide film from the center to the periphery of the arc.

Here, periodic variable heat source distribution parameters and thermal efficiencies are used to realize the output heat variation of the VPPA arc. The combined heat source model is schematically shown in Fig.4.

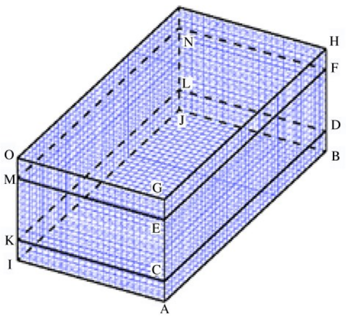

Fig.2 Schematic diagram of the surface boundary

Table 4 Surface boundary conditions

Boundary	Momentum	Thermal energy
EFNM	$\vec{v} = 0$	$\kappa(\partial T/\partial \vec{n}) = -h_c(T - T_0) - \sigma\varepsilon(T^4 - T_0^4)$
CDLK	$\vec{v} = 0$	$\kappa(\partial T/\partial \vec{n}) = -h_c(T - T_0) - \sigma\varepsilon(T^4 - T_0^4)$
CEKM	$\vec{v} = 0$	$\kappa(\partial T/\partial \vec{n}) = -h_c(T - T_0)$
KLNM	$\vec{v} = 0$	$\kappa(\partial T/\partial \vec{n}) = -h_c(T - T_0)$
DFNL	$\vec{v} = 0$	$\kappa(\partial T/\partial \vec{n}) = -h_c(T - T_0)$
ABHG	$\vec{v} = 0$ $\partial u/\partial \vec{y} = 0$ $\partial w/\partial \vec{y} = 0$	$\partial T/\partial \vec{y} = 0$

The heat source model S_v consists of a double ellipsoid heatsource[30] on the top and a logarithmic curve rotating body heat source with linearly increasing peak value[31] below. The asymmetry of the double ellipsoid heat source distribution exactly reflects the asymmetry of the weld pool caused by gravity. The logarithmic curve rotating body heat source model with linearly increasing peak value can meet the characteristics of increasing heat flux along the thickness direction due to the secondary compression of the keyhole.

The heat flux distribution of the double ellipsoid heat source is described as follows:

$$\begin{cases} q_\mathrm{f} = \dfrac{12\sqrt{3}\, UIm_1 \eta f_1}{\pi\sqrt{\pi}\, a_\mathrm{f} bc} \exp\left(\dfrac{-3x^2}{a_\mathrm{f}^2} - \dfrac{-3y^2}{b_\mathrm{h}^2} - \dfrac{-3z^2}{c_\mathrm{h}^2}\right) & x > 0,\ -0.006 < z \leqslant 0 \\ q_\mathrm{r} = \dfrac{12\sqrt{3}\, UIm_1 \eta f_2}{\pi\sqrt{\pi}\, a_\mathrm{r} bc} \exp\left(\dfrac{-3x^2}{a_\mathrm{r}^2} - \dfrac{-3y^2}{b_\mathrm{h}^2} - \dfrac{-3z^2}{c_\mathrm{h}^2}\right) & x \leqslant 0,\ -0.006 < z \leqslant 0 \\ (\text{EN phase: } I = I_\mathrm{en}, U = U_\mathrm{en}, \eta = \eta_\mathrm{en}, a_\mathrm{r} = a_\mathrm{ren}, a_\mathrm{f} = a_\mathrm{fen}, b_\mathrm{h} = b_\mathrm{hen}, c_\mathrm{h} = c_\mathrm{hen}) & \\ (\text{EP phase: } I = I_\mathrm{ep}, U = U_\mathrm{ep}, \eta = \eta_\mathrm{ep}, a_\mathrm{r} = a_\mathrm{rep}, a_\mathrm{f} = a_\mathrm{fep}, b_\mathrm{h} = b_\mathrm{hep}, c_\mathrm{h} = c_\mathrm{hep}) & \end{cases} \tag{20}$$

where $a_\mathrm{f}, a_\mathrm{r}, b_\mathrm{h}, c_\mathrm{h}$ are the distribution parameters of the double ellipsoid heat source.

The heat flux distribution of the curve rotating body heat source model with linearly increasing peak value can be described by Eq.(21).

$$\begin{cases} q_\mathrm{v} = Q_0\left(\dfrac{1-x}{z_\mathrm{e} - z_i} z - \dfrac{1-x}{z_\mathrm{e} - z_i} z_\mathrm{e} + 1\right) \exp\left(-\dfrac{3r^2}{\left(\dfrac{r_\mathrm{e} - r_i}{\ln z_\mathrm{e} - \ln z_i} \ln z + \dfrac{r_i \ln z_\mathrm{e} - r_\mathrm{e} \ln z_i}{\ln z_\mathrm{e} - \ln z_i}\right)^2}\right) & -0.012 \leqslant z \leqslant -0.006 \\ Q_0 = \dfrac{3UI\eta m_2}{\pi(1 - \mathrm{e}^{-3})\left[\dfrac{1-\zeta}{z_\mathrm{e} - z_i}(A + B + C) + \left(1 - \dfrac{1-x}{z_\mathrm{e} - z_i} z_\mathrm{e}\right) D\right]} & \\ (\text{EN phase: } I = I_\mathrm{en}, U = U_\mathrm{en}, \eta = \eta_\mathrm{en}, m_2 = m_\mathrm{2en}, r_\mathrm{e} = r_\mathrm{een}, r_\mathrm{i} = r_\mathrm{ien}) & \\ (\text{EP phase: } I = I_\mathrm{ep}, U = U_\mathrm{ep}, \eta = \eta_\mathrm{ep}, m_2 = m_\mathrm{2ep}, r_\mathrm{e} = r_\mathrm{eep}, r_\mathrm{i} = r_\mathrm{iep}) & \end{cases} \tag{21}$$

where z_e and z_i are the z coordinates for the top and bottom heat source surface, respectively; ζ is the adjustment coefficient of heat flux density along the thickness direction of the workpiece; A, B, C, and D are the calculation coefficients.

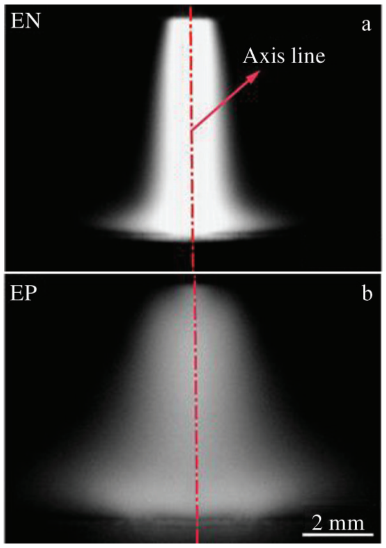

Fig.3 Captured arc shape in the EN (a) and EP (b) phases

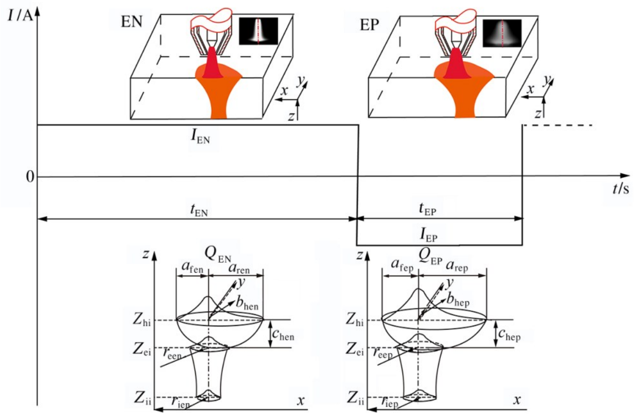

Fig.4 Schematic diagram of the heat source distribution in the EN and EP phase

The heat source distribution parameters are initially determined according to the size of the weld pool. Fig. 3 shows that the distribution range of the arc in EP phase is about 1.5 times larger than that in EN phase. Thus, $a_{fep} = 1.5a_{fen}$, $b_{hep} = 1.5b_{hen}$, $c_{hep} = 1.5c_{hen}$, $r_{eep} = 1.5r_{een}$, $r_{iep} = 1.5r_{ien}$. The heat source distribution parameters are finally determined though debugging. Han[32] et al proposed that EP phase is twice as efficient as EN phase. Namely, $2U_{en}I_{en}\eta_{en} = U_{ep}I_{ep}\eta_{ep}$ and $\eta_{ep} \approx 1.5\eta_{en}$.

The average efficiency is 0.55 used in Ref.[21], so, here set $\eta_{ep} = 0.66$ and $\eta_{en} = 0.44$.

2.5 Arc pressure for VPPAW process

The arc pressure model was always developed as follows[9]:

$$\begin{cases} P_a = \dfrac{\mu_0 I^2}{4\pi^2}\left[\left(\dfrac{1}{r_2^2 - r_1^2}\right) + \dfrac{c_j}{2\sigma_j^2}\exp\left(\dfrac{-r^2}{2\sigma_j^2}\right)\right] \\ (\text{EN phase: } I = I_{en}, r_1 = r_{1en}, r_2 = r_{2en}) \\ (\text{EP phase: } I = I_{ep}, r_1 = r_{1ep}, r_2 = r_{iep}) \end{cases} \tag{22}$$

where r_1 and r_2 are the plasma arc radii on the workpiece and at the nozzle, respectively.

Wu proposed that the keyhole has secondary compression effect on heat flux and arc pressure in VPPAW[14,19]. Assuming that the keyhole begins to appear at time of t_{p0} and is penetrated at time of t_{p1}. The arc pressure model P_a can be improved as follows:

$$P_a' = P_a \times (1 + \varphi(\frac{h_{kh}}{L})^2)C_j'(t_{p0} \leqslant t \leqslant t_{p1}) \tag{23}$$

where φ is more than zero and less than one and is introduced to consider the variation of the arc pressure with the change of weld pool depth, C_j' is introduced to consider the influence of different VPF on the arc pressure.

The arc in EP phase is gradually divergent due to cathode cleaning. The divergence time is shortened with increasing the VPF. In addition, the thermal inertia of arc makes the change of arc lag the change of current, which further shortens the expansion time of the arc. So, the arc distribution range in EP phase is reduced. Cong[33] et al reported that arc is essentially a kind of gaseous conductor composed of charged particles, and there is interaction force between the charged particles. With increasing the VPF, the increased force between particles makes the arc contracted. Here it is assumed that the distribution parameters of heat source and arc pressure decrease linearly by 0.05 times with increasing the VPF.

2.6 Simulation consideration

The size of established computational domain is 30 mm in length (x-axis), 15 mm in width (y-axis) and 16 mm in thickness (z-axis), which is divided into three layers, namely air layer, metal layer and air layer from top to bottom. The thickness of the air layer and the metal layer is 2 and 12 mm, respectively. The minimum mesh size is 0.3 mm. The governing differential equations are solved by the PISO algorithm. The convergence criteria for the sum of the normalized residues have been set to be 10^{-3} for the continuity and momentum equations and 10^{-6} for the energy equation. The time step of 5×10^{-5} s was used to track the keyhole accurately. The main thermo-physical properties of AA2A14 are set in Table 5.

3 Results and Discussion

3.1 Simulation results

Fig. 5 shows that the arc pressure of the weld pool in EN phase is larger and more concentrated than that of EP phase, and the peak value of the arc pressure generally decreases from 7930 Pa to 6020 Pa and from 7110 Pa to 5820 Pa in the EN and EP phase, respectively as the VPF increases (here, a complete variable-polarity time period corresponding to 2.5 s is taken for comparison). The range of arc pressure values is basically consistent with the study of Han[34], which confirms the accuracy of the arc pressure model. What's more, the difference become smaller (from 820 Pa to 200 Pa) as the VPF increases.

The contours of the heat flux distribution on the weld pool show that the peak value of the heat flux in EN phase is larger and more concentrated than in EP phase, and the difference

Table 5 Thermo-physical properties of AA2A14[24]

Parameter	Value	Temperature/K
C_p/J·kg^{-1}·K^{-1}	838	646
	880	746
	964	846
	1090	946
k/W·(m·K)$^{-1}$	168	646
	176	746
	180	846
	180	946
μ/×10^{-3} kg·m^{-1}·s^{-1}	1.18	943
	1.0	973
	0.8	1023
h_c/W·m^{-2}· K^{-1}	40	300
	60	500
	80	800
	80	1000

becomes smaller (from 4×10^9 W·mm^{-2} to 9×10^8 W·mm^{-2}) as the VPF increases.

Fig. 6 shows that the flow velocity in EN phase is higher than in EP phase, and the flow velocity decreases and the difference becomes smaller with increasing the VPF.

The VPFs in Fig. 7 are 27, 33, 41, 83 and 166. The arc pressure ΔP, heat flux ΔHF, flow velocity ΔV of the weld pool decrease from 820 Pa to 200 Pa, 4×10^9 W·m^{-2} to 9×10^8 W·m^{-2}, and 0.4 m·s^{-1} to 0.1 m·s^{-1}, respectively with increasing the VPF.

To sum up, the thermal-mechanical "oscillation intensity" at the keyhole boundary is generally reduced as the VPF increases, which is conducive to maintaining the weld pool stability.

Fig. 8a shows that the workpiece surface is first heated and an arc crater forms. With the accumulation of heat, the expanded molten metal flows upward from the center to the upper edge of the weld pool under the action of arc pressure and surface tension. At 2.13 s, the weld pool with a width of 3 mm and a depth of 2 mm is formed. Under the thermal-mechanical coupling of the arc, the sizes of the weld pool and the keyhole increase. The increasing rate of weld width and depth decreases gradually (from 0.43 to 0.08 and 0.89 to 0.22, respectively). At 3.36 s, the workpiece is penetrated and form a melting bridge, and it takes about 0.11 s for the melting bridge to be penetrated. The molten metal in the bottom of the weld pool flows downwards and outwards, shown as ① in Fig. 8f, at the maximum velocity of 0.8 m/s. The weld pool

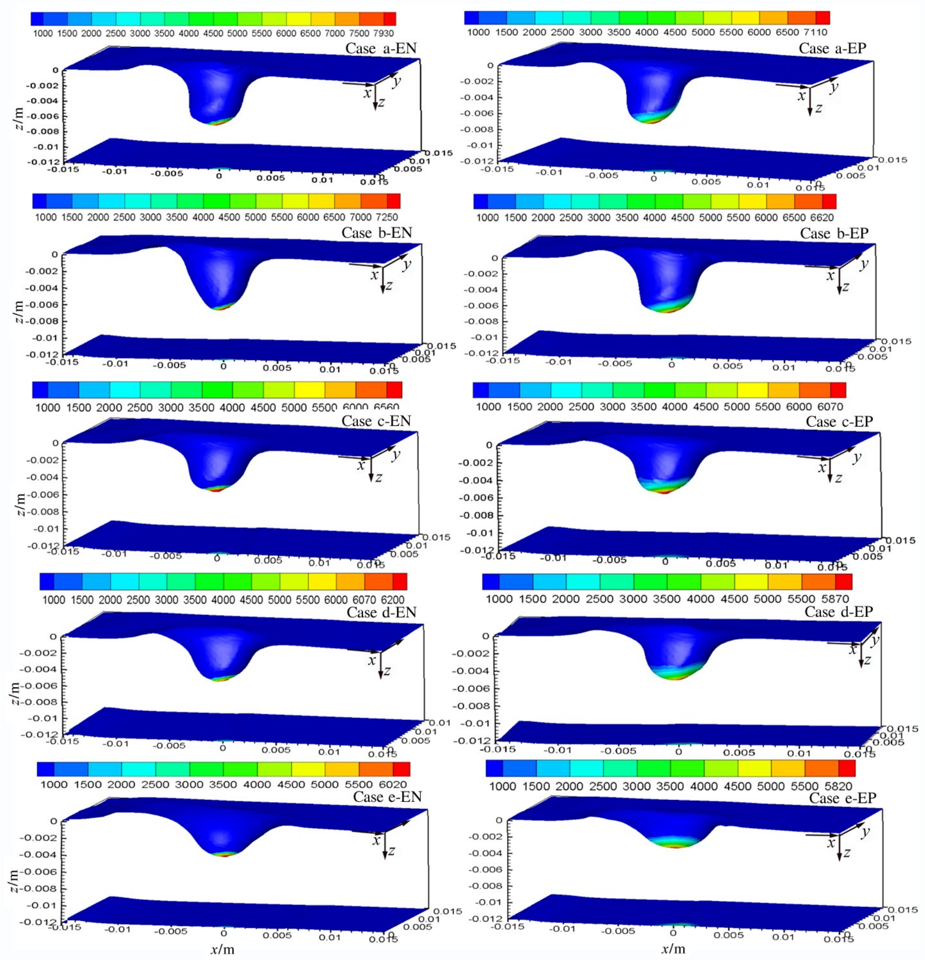

Fig.5 Arc pressure distribution in EN and EP phase as the VPF increases in different cases

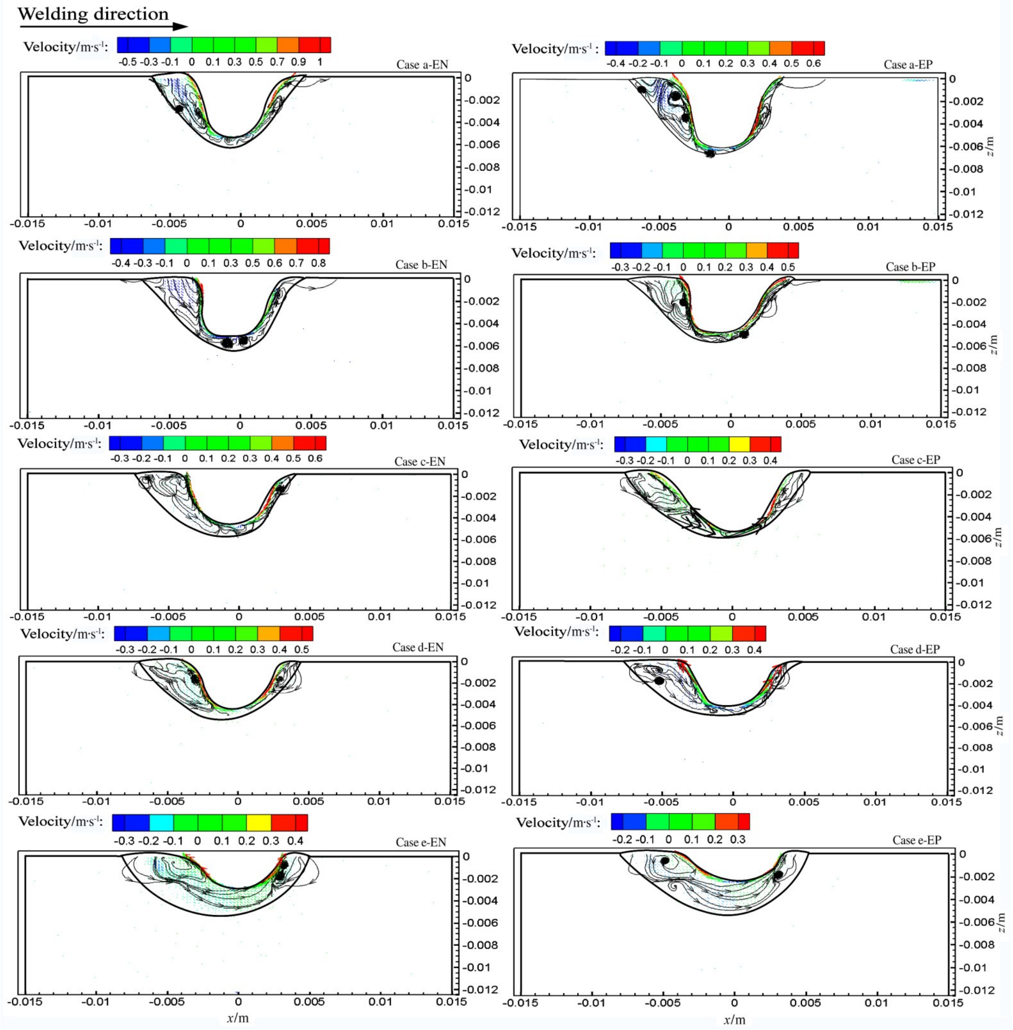

Fig.6 Flow velocity in the weld pool in the EN and EP phase as the VPF increases in different cases

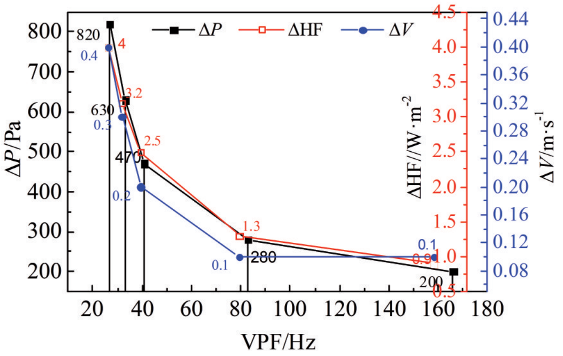

Fig.7 Variation of arc pressure, heat flux and flow velocity at the keyhole boundary with different VPFs

temperature at the line of $z=-10$ mm is selected as a reference to calculate the temperature gradient of the bottom weld pool, and the temperature gradient is 133 K/mm when the VPF is 27.

Fig. 9 shows that the penetration time increases and the maximum flow velocity at the bottom of the weld pool decreases with increasing the VPF.

Fig. 10 shows that the weld pool temperature gradient decreases and the highest temperature of the bottom weld pool increases with increasing the VPFs due to the prolonged heating time of the weld pool.

3.2 Experimental results

As shown in Fig.11 when the VPF is 27, the top side of the weld is uneven, and the back-side of the weld is cut intermittently. The weld pool is stable when the VPFs are between 33 and 83. When the frequency is 166, the weld pool is unstable and discontinuous bulges appear on the back of the weld.

3.3 Discussion

As shown in Fig. 12b, the gravity F_g of the molten bridge increases when the surface tension F_s decreases with increasing the VPFs. This is because there is a large amount of molten metal in the front molten bridge, and the temperature gradient decreases due to the prolonged perforation time. In addition, P'_a decreases with increasing VPF, which makes the curvature radius of the bottom boundary of the weld pool decrease, and the additional pressure P_t increases. In the

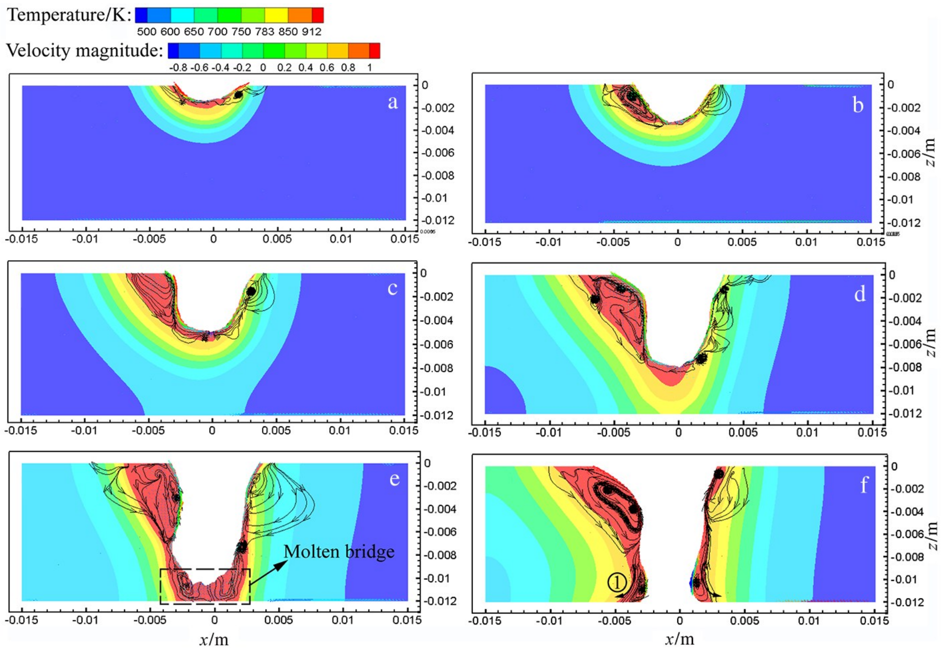

Fig.8 Temperature and material flow fields on longitudinal section of the keyhole weld pool in Case-a: (a) 2.13 s, (b) 2.34 s, (c) 2.69 s, (d) 3.05 s, (e) 3.36 s, and (f) 3.47 s

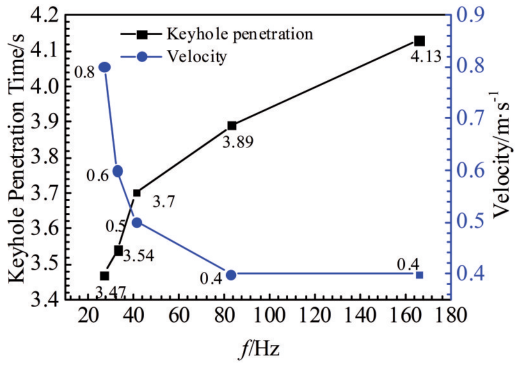

Fig.9 Weld pool penetration time and the maximum flow velocity at the bottom of weld pool with increasing the VPF

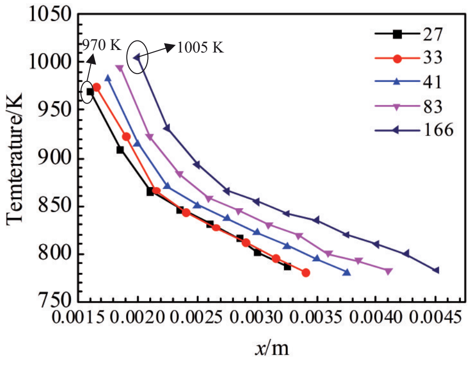

Fig.10 Temperature distribution of the bottom weld pool at different VPFs

critical state of the molten bridge being penetrated, the force state of the front molten bridge is crucial to the weld pool stability. The resultant force of P_a' and F_s which promote the keyhole expansion is larger than that of F_g and P_t which accelerate the keyhole closure if VPFs are less than 33. In addition, the arc shear force τ is large, and the molten metal rushes out of the weld pool at a high velocity (0.8 m/s). According to the law of mass conservation, the weld pool tends to be cut, as shown in Fig.11. When VPF is larger than 83, the resultant force of F_g and P_t is larger than that of P_a' and F_s, the heat and arc pressure is accumulated, resulting in bulges on the back of the weld. The molten bridge is penetrated when P_a' accumulates to a certain extent, then P_a' drops dramatically (molten bridge is penetrated and the P_a' is released) and it is necessary to accumulate the heat and force at the bottom of the molten bridge to realize the next penetration. So as to cycle, discontinuous bulges form, as shown in Fig.11 when the VPF is 166.

3.4 Experimental validation

The test plates were sectioned, and metallographic treatments were implemented to reveal the fusion line boundary. Fig. 13 shows a comparison between the experimental macro morphology of the welded joints and the calculated ones. Here, liquidus (T=783 K) is used as the fusion line of AA2A14 aluminum alloy. Detailed comparative data are shown in Table 6.

The results show that the deviation between the calculated and measured sizes of the front and back weld pool is less than 3%, that is, the calculated fusion lines are in good agreement with the experimental ones. The accuracy of the thermal-mechanical coupling model established is verified.

Fig. 14 shows that the experimentally measured and calculated keyhole dimensions of the bottom agree well (the relative error of measured and simulated keyhole width and

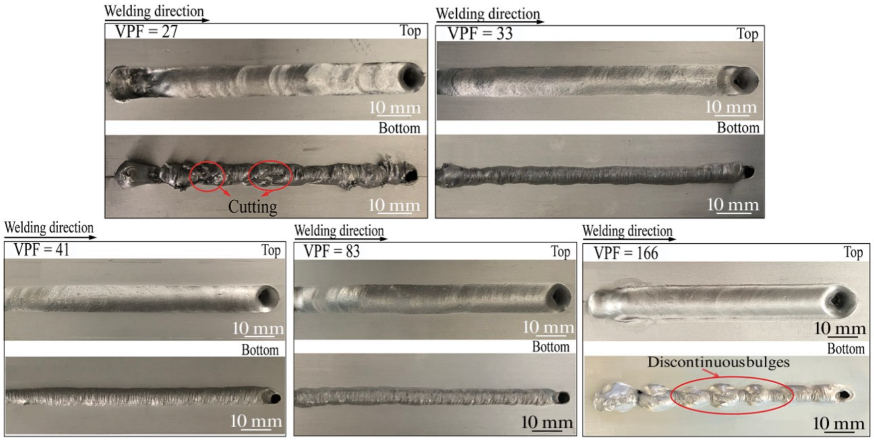

Fig.11 Weld formations with increasing the VPF

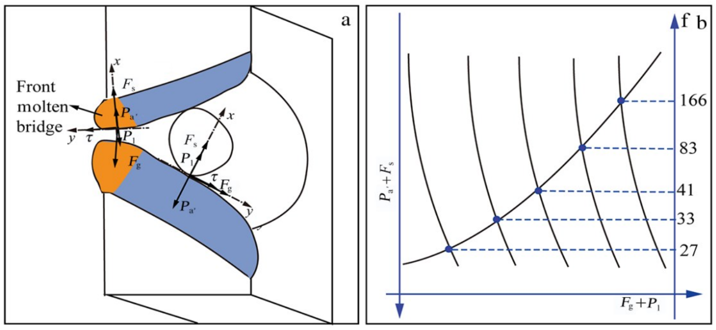

Fig.12 Schematic of force state of the molten pool (a) and force balance analysis of the molten bridge with different VPF (b)

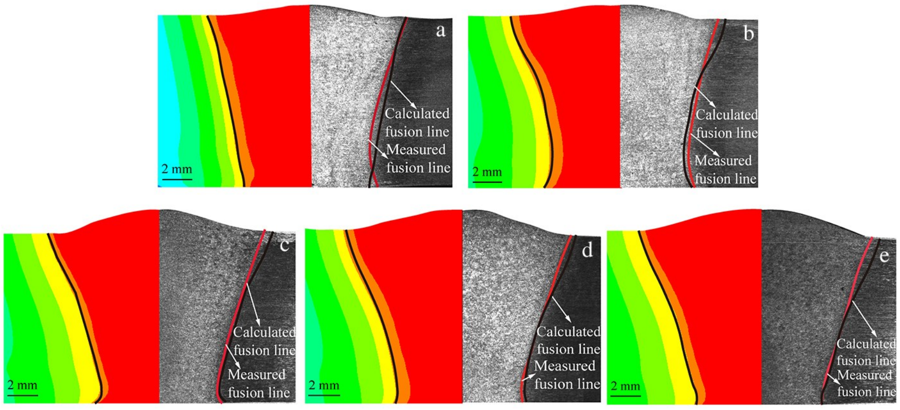

Fig.13 Comparison between calculated results of the fusion zone and experimental macromorphology of the welded joints at the transverse cross-section of the weld beads: (a) VPF=27, (b) VPF=33, (c) VPF=41, (d) VPF=83, and (e) VPF=166

Table 6 Comparison of the front and back dimensions of the weld pool

Case	Measured/mm		Calculated/mm		|Relative Error|/%	
	Front	Back	Front	Back	Front	Back
a	12.11	9.03	12.25	8.83	1.16	2.21
b	13.35	9.55	13.14	9.34	1.60	2.22
c	13.82	7.68	13.96	7.76	1.01	1.04
d	13.53	6.89	13.67	6.98	1.03	1.30
e	14.05	7.02	13.88	7.23	1.21	2.99

length are 4.6% and 8.5%, respectively). The deviations of keyhole width and length of Case a~e are within 8.0% and 8.5%, respectively.

In addition, the experimental keyhole image of the back of the weld beam captured by the high-speed camera agrees well with the calculated ones. The relative errors of measured and simulated keyhole width and length are 4.6% and 8.5%, respectively. As shown in Table 7, the deviations of keyhole width and length in Case a~e are within 8.0% and 8.5%, respectively, which further verifies the accuracy of the

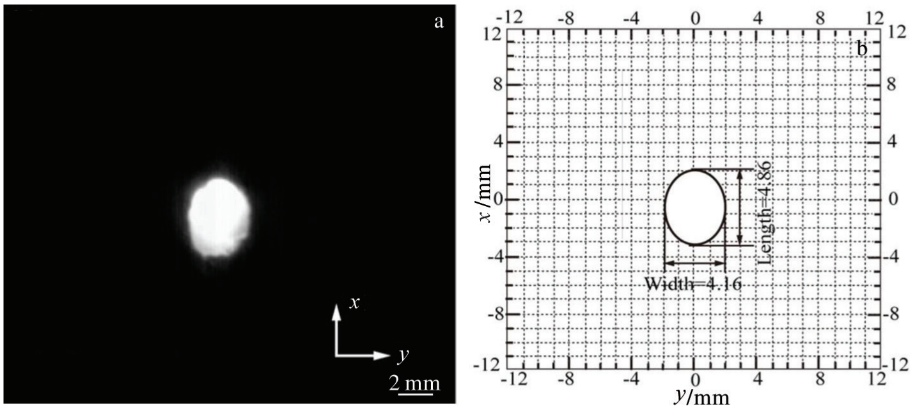

Fig.14 Comparison between experimental image (a) and calculated result (b) of the keyhole geometry of the bottom in Case-a

Table 7 Comparison of the keyhole penetration time and the back size of the keyhole width and length

Case	Measured/Calculated			|Relative Error|/%		
	Keyhole penetration time/s	Keyhole width on the bottom/mm	Keyhole length on the bottom/mm	Keyhole penetration time	Keyhole width on the bottom	Keyhole length on the bottom
a	3.47/3.75	4.36/4.16	4.80/5.21	8.0	4.6	8.5
b	3.51/3.69	4.37/4.09	4.76/5.13	5.1	6.4	7.8
c	3.70/3.88	4.28/4.43	4.74/5.05	4.9	3.5	6.5
d	3.89/4.11	4.25/4.38	4.63/4.82	5.7	3.1	4.1
e	4.13/4.36	4.12/4.40	4.61/4.89	5.6	6.1	6.1

thermal-mechanical coupling model.

4 Conclusions

1) The variable-polarity finite element model can be used to reveal the impacting mechanism of variable polarity frequency (VPF) on the weld pool stability in variable polarity plasma arc welding (VPPAW).

2) The model can realize the periodic variation of thermal and mechanical effects of variable polarity arc on the weld pool. Moreover, the secondary compression effect of the keyhole on heat flux and arc pressure is taken into account.

3) The thermal-mechanical "oscillation intensity" on the weld pool is weakened with increasing the VPF, which is beneficial to the weld pool stability.

4) When the VPFs are more than 33 and less than 83, the thermal-mechanical "oscillations intensity" at the keyhole boundary is weak, and the molten bridge can stay force balance in the critical state of being penetrated. The weld pool can maintain stable.

5) When the VPFs are less than 33, the resultant force of P_a' and F_s is larger than that of F_g and P_t. In addition, the arc shear force τ is large, and the molten metal rushes out of the weld pool at a high velocity (0.8 m/s). According to the law of mass conservation, the weld pool tends to be cut.

6) If VPFs are larger than 83, the resultant force of F_g and P_t is larger than that of P_a' and F_s, and the heat and arc pressure are accumulated, which makes bulges on the back of the weld. The molten bridge is penetrated when P_a' is accumulated to a certain extent, then P_a' drops dramatically and it is necessary to accumulate the heat and force at the bottom of the molten bridge to realize the next penetration. The weld pool is unstable.

References

1 Jenney C L, O'Brien A. *Welding Handbook*[M]. Miami: American Welding Society, 2001: 303

2 Liu Z H, Zhao B, Zhao Q. *Missiles and Space Vehicles*[J], 2002, 5: 63 (in Chinese)

3 Chen K X, Li H Q, Li C X. *Transactions of the China Welding Institution*[J], 2004, 25(1): 124

4 Yao J S, Xu M, Jia H D *et al*. *Aeronautical Manufacturing Technology*[J], 2008, 8: 32 (in Chinese)

5 Han Y Q, Chen S J, Yin S Y *et al*. *Journal of Mechanical Engineering*[J], 2006, 42(9): 144

6 Han Y Q, Guo L, Chen S J *et al*. *Journal of Materials Engineering*[J], 2011, 12: 83

7 Li G W, Chen F R, Han Y Q *et al*. *Welding Technology*[J], 2015, 44(11): 29 (in Chinese)

8 Liu J, Yao J S, Guo L J. *Aeronautical Manufacturing Technology* [J], 2008, 8: 74 (in Chinese)

9 Chen S J, Xu B, Jiang F. *International Journal of Heat and Mass Transfer*[J], 2018, 118: 1293

10 Xu B, Chen S J, Jiang F *et al*. *Journal of Manufacturing Processes*[J], 2019, 37: 519

11 Pei L C. *Thesis for Master*[D]. Harbin: Harbin Institute of Technology, 2006

12 Murphy A B. *Plasma Chemistry and Plasma Processing*[J], 2015, 35: 471

13 Nguyen A V, Wu D S, Tashiro S *et al*. *Welding Journal*[J], 2019, 98: 202

14 Wu D S, Anh V N, Tashiro S *et al*. *International Journal of Heat and Mass Transfer*[J], 2019, 131: 920

15 Yan Z Y, Chen S J, Jiang F *et al*. *Journal of Manufacturing Processes*[J], 2018, 36: 480

16 Wang H X, Wei Y H, Yang C L. *Computational Materials Science*[J], 2007, 38(4): 571

17 Wang H X, Wei Y H, Yang C L. *Computational Materials Science*[J], 2007, 40(2): 213

18 Wang H X, Wei Y H, Yang C L. *Science and Technology of Welding & Joining*[J], 2007, 12(1): 32

19 Xu B, Jiang F, Chen S J *et al*. *Chinese Physics B*[J], 2018, 27(3): 306

20 Shang Jing, Wang Kehong, Zhou Qi *et al*. *Rare Metal Materials and Engineering*[J], 2013, 42(7): 1337

21 Zhang Q L, Yang C L, Lin S B *et al*. *Transactions of the China Welding Institution*[J], 2013, 34(9): 79

22 Li Y, Feng Y, Zhang X *et al*. *Energy*[J], 2014, 64: 1044

23 Bennon W D, Incropera F P. *International Journal of Heat and Mass Transfer*[J], 1987, 30(10): 2161

24 Practical Handbook of Engineering Materials Editorial Committee. *Practical Handbook of Engineering Materials*[M]. Beijing: China Standard Press, 1989: 214

25 Li T Q, Wu C S. *International Journal of Advanced Manufacturing Technology*[J], 2015, 78(1): 593

26 Zhang T, Wu C S, Feng Y. *Numerical Heat Transfer Part A Applications*[J], 2011, 60(8): 685

27 Li Y, Feng Y, Zhang X *et al*. *International Journal of Thermal Sciences*[J], 2013, 64: 93

28 Bai X, Colegrove P, Ding J *et al*. *International Journal of Heat and Mass Transfer*[J], 2018, 124: 504

29 Brackbill J U, Kothe D B, Zemach C. *Journal of Computational Physics*[J],1992, 100(2): 335

30 Goldak J, Chakravarti A, Bibby M. *Metallurgical Transactions B* [J],1984, 15(2): 299

31 Xu G, Wu C, Qin G *et al*. *Acta Metallurgica Sinica*[J], 2008, 44(4): 478

32 Han Y Q, Yin S Y, Chen S J. *Transactions of the China Welding Institution*[J], 2007, 28(12): 35

33 Cong B, Qi B, Zhou X. *Transactions of the China Welding Institution*[J], 2009, 30(6): 87

34 Han Y Q, Lu Y H, Chen S J *et al*. *Electric Welding Machine*[J], 2005, 2: 54

变极性频率对铝合金变极性等离子弧穿孔立焊熔池稳定性的影响机理

郎瑞卿，韩永全，白雪宇，包蓄磊

(内蒙古工业大学，内蒙古 呼和浩特 010051)

摘　要：为研究变极性频率（VPF）对变极性等离子弧焊熔池稳定性的影响机理，采用变极性有限元模型分析了小孔熔池的热力耦合过程。该模型基于计算流体力学（CFD）技术，能够实现变极性电弧对熔池热-力作用的周期性变化。此外，为了更准确地表达小孔边界上热量和力分布沿小孔深度的变化，还考虑了小孔的二次压缩效应对热流和电弧压力的影响。比较了不同VPFs条件下小孔边界的热-力振荡强度和熔融桥在临界穿透时的受力平衡情况。结果表明，在小孔形成过程中，随着VPFs的增大，小孔边界的电弧压力、热流密度和流动速度的“振荡强度”减小。另外，不同的热-力振荡条件引起熔池温度场的变化，进而导致熔池表面张力的变化，改变了熔融桥在穿透时的受力平衡条件，影响穿孔熔池的稳定性。当EP相电流占空比为1/5，VPFs大于33，小于83时，匙孔边界的热-力“振荡强度”较弱，熔融桥在临界熔透状态下能保持力平衡，熔池稳定。当VPFs小于33时，“振荡强度”较强，并且熔融桥的受力平衡被打破，熔池趋于被切割。当VPFs大于83时，虽然此时熔融桥“振荡强度”较弱，但因熔融桥受力平衡被打破，熔池处于不稳定状态。最后，通过熔合线形状、小孔穿透时间和焊缝背面小孔尺寸的比较，验证了所建立模型的准确性。

关键词：变极性等离子弧焊接；变极性频率；匙孔压缩效应；热-力振荡；熔池稳定性

作者简介：郎瑞卿，女，1988年生，博士，内蒙古工业大学材料科学与工程学院，内蒙古 呼和浩特 010051，E-mail：langruiqing2@163.com